Research Square

Preprints are preliminary reports that have not undergone peer review.
They should not be considered conclusive, used to inform clinical practice,
or referenced by the media as validated information.

Synergistic Engineering of Fluorine Doping $Fe_xMn_{1-x}MoO_4$/Graphene Heterojunction as Ultrahigh-Rate Anode for LIBs

Tianwei Liu
Xiangnan University
Xiaomin Chen
Xiangnan University
Huiling Chen
Xiangnan University
Caiyong Huang
Central Blood Station
Pu Yu
Xiangnan University
Wei Tang
t153675772690163.com

Xiangnan University

Article

Keywords: FexMn1−xMoO4/G anode materials, fluorine doping, ultrahigh rate, heterojunction structure, synergistic enhancement

Posted Date: April 8th, 2026

DOI: https://doi.org/10.21203/rs.3.rs-9264724/v1

License: This work is licensed under a Creative Commons Attribution 4.0 International License.
Read Full License

Additional Declarations: No competing interests reported.

Version of Record: A version of this preprint was published at Scientific Reports on May 28th, 2026. See the published version at https://doi.org/10.1038/s41598-026-55355-6.

Abstract

The development of advanced anode materials is critical for high-energy and high-power lithium-ion batteries (LIBs). Conventional conversion-type anodes, such as transition metal molybdates, suffer from poor conductivity, severe volume expansion, and structural degradation, leading to rapid capacity fading. To overcome these limitations, we propose a synergistic design strategy that integrates heterojunction engineering with fluorine doping. A fluorine-doped, heterojunction-structured F-$Fe_xMn_{1-x}MoO_4$/graphene (F-FMMO/G) was successfully synthesized via a facile solvothermal route. Structural characterizations confirm the formation of a well-defined $FeMoO_4/Mn_2Mo_3O_8$ heterojunction with effective fluorine incorporation. When evaluated as an anode for LIBs, the F-FMMO/G composite exhibits an ultrahigh initial specific capacity of 1158 mAh g^{-1} at 0.1 C and maintains 780 mAh g^{-1} after 150 cycles, substantially outperforming the undoped counterpart. Notably, it delivers excellent rate performance, sustaining ~ 100 mAh g^{-1} at 10 C and rapidly recovering to > 900 mAh g^{-1} when cycled back to 0.1 C. The enhanced electrochemical performance is attributed to the synergistic effects of the built-in electric field at the heterojunction interface, which promotes rapid charge transfer, and fluorine doping, which optimizes the electronic structure and stabilizes the electrode–electrolyte interface. This study offers a rational design framework combining interfacial and bulk modifications for next-generation high-rate LIB anodes.

Introduction

The growing demand for lithium-ion batteries (LIBs) with both high energy and power densities has spurred intense research into advanced anode materials beyond conventional graphite. Among the most promising candidates are transition metal oxides (TMOs) and molybdates, which offer high theoretical capacities via multi-electron conversion reactions[1,2]. However, their practical application is hindered by several intrinsic limitations, including low electronic conductivity, significant volume changes during lithiation/delithiation, and resulting structural pulverization and rapid capacity decay[3,4].

To address these challenges, heterojunction engineering has emerged as a key strategy in advanced electrode design. A heterojunction, formed at the interface between two semiconductors with distinct band structures, generates a built-in electric field that facilitates directional charge separation and transport. This interfacial electric field acts as a nanoscale ‘highway’, significantly enhancing charge-transfer kinetics and mitigating the conductivity bottleneck[5,6]. Additionally, the mechanical interplay between the constituent phases can relieve internal stress during cycling. One phase may serve as a structural buffer or conductive scaffold for the other, thereby reducing volume expansion and preserving structural integrity, which is critical for achieving long-term cyclability[7,8]. Notably, recent studies on Co_3O_4/ZnO, Fe_2O_3/SnO_2, and $NiCo_2O_4/MnO_2$ heterostructures have demonstrated enhanced rate capability and improved mechanical stability compared to their single-phase analogs[9–11]. Elemental doping, particularly with anions such as fluorine (F), offers a complementary avenue for tailoring the physicochemical properties of electrode materials. F-doping induces lattice distortion, introduces

oxygen vacancies, and modifies the electronic band structure, collectively improving both ionic and electronic conductivity[12,13]. Moreover, the formation of strong metal-fluorine (M–F) bonds at the surface generates a robust interfacial layer that stabilizes the solid-electrolyte interphase (SEI) and suppresses unwanted side reactions during extended cycling[14,15]. The combination of heterojunction engineering and targeted doping thus presents a synergistic strategy: the heterojunction enhances charge transport and structural resilience, while doping optimizes surface chemistry and electronic structure[16,17]. Iron molybdate ($FeMoO_4$) and manganese molybdate ($MnMoO_4$) are environmentally benign materials with high theoretical capacities, making them attractive for LIB anodes. Nevertheless, their individual electrochemical performance is limited by poor conductivity and structural degradation upon cycling[18,19]. A $Fe_xMn_{1-x}MoO_4$-based heterojunction can leverage the benefits of both parent compounds. While molybdate-based heterostructures such as MoO_2/MoS_2 and $CoMoO_4/NiMoO_4$ have shown promise in boosting electrochemical kinetics[20], the specific integration of a fluorine-doped $FeMoO_4/Mn_2Mo_3O_8$ heterojunction with conductive graphene remains largely unexplored[21].

In this study, we design and synthesize a fluorine-doped, heterojunction-structured $Fe_xMn_{1-x}MoO_4$/graphene (F-FMMO/G) nanocomposite via a facile solvothermal method. The work aims to elucidate how the combined strategies of heterojunction formation and fluorine doping jointly address the limitations of conversion-type anodes. We systematically investigate improvements in structural stability (e.g., buffered volume changes and robust SEI formation), charge transfer efficiency (e.g., reduced interfacial resistance and enhanced conductivity), and overall electrochemical kinetics. Advanced characterizations, supported by density functional theory (DFT) simulations, reveal the fundamental mechanisms underlying the ultrahigh-rate performance and superior cycling stability. This work establishes a rational design blueprint that couples interfacial and bulk modifications for next-generation high-power LIB anodes.

Results and Discussions

Thermal stability of the precursor

Figure 1a presents the TG-DSC curves of the FMMO precursor heated under N_2 from room temperature to 800 ℃, which reveals the thermal behavior and crystallization temperature. As the temperature increases, a gradual mass loss is observed, accompanied by endothermic behavior. A distinct exothermic peak appears at approximately 400 ℃, corresponding to the formation of crystalline phases and a sharp weight loss of over 7%, indicating a major decomposition and crystallization step associated with oxide phase formation. Following this step, a slower and continuous weight loss process ensues, resembling thermal behavior before 400 ℃. As heating continues, a second exothermic peak is detected at 730 ℃, suggesting the onset of more complex phase transformations. Based on these observations, a calcination temperature of 650 ℃ was selected to obtain well-crystallized products while avoiding the higher-temperature regime where more complex phase transformations

may occur.

XRD and Morphology Comparison of FMMOs

Figure 1b displays the X-ray diffraction (XRD) patterns of FMMO/G and F-FMMO/G composites calcined at 650 ℃. Both samples exhibit mixed-phase structures, indicating that neither is a single-phase material. The diffraction pattern of FMMO/G shows three prominent peaks: the reflections at 2θ ≈ 26.5° corresponding to the (220) plane of $FeMoO_4$ (JCPDS 22–628), while peaks at 37° and 53° corresponding to the (201) and (006) planes of $Mn_2Mo_3O_8$ (JCPDS 34–510), respectively. Upon fluorine doping, the F-FMMO/G sample exhibits enhanced crystallinity, as evidenced by increased peak intensity and additional diffraction peaks. In addition to the $FeMoO_4$ (220) peak, several new $Mn_2Mo_3O_8$ peaks appear at 15° (002), 25.5° (102), 36° (112), and 45° (203), indicating the formation of an improved crystallinity and ordered heterostructure. To further elucidate the structural evolution, Raman spectroscopy was conducted on both samples, as shown in Fig. 1c. Both FMMO/G and F-FMMO/G exhibit characteristic D and G graphene bands at 1347 cm^{-1} and 1597 cm^{-1}, respectively. Notably, the relative intensity of these bands decreases after fluorine doping, indicating stronger coupling between the carbon framework and the fluorine-modified oxide matrix, along with changes in defect density within the carbon component. Peaks at 199 cm^{-1} and 347 cm^{-1}, attributed to the Fe–O stretching vibration and the triply degenerate bending vibration of the MoO_4 tetrahedra, respectively, are present in both samples. Upon fluorine doping, new peaks emerge in the Raman spectrum of F-FMMO/G: a prominent peak at 819 cm^{-1} assigned to the asymmetric stretching vibration of MoO_4 tetrahedra[21], as well as additional peaks at 931 cm^{-1} and 992 cm^{-1} corresponding to the symmetric stretching modes of terminal metal–oxygen (M = O) bonds. The appearance of these new peaks, combined with an overall increase in peak intensity, reflects enhanced crystallinity and a more mature phase structure in the fluorine-doped sample.

Electrochemical Performance

Electrochemical impedance spectroscopy (EIS) analysis of both samples is shown in Fig. 1d. The Nyquist plots feature a depressed semicircle in the high-frequency region, indicative of charge-transfer resistance, and a linear tail in the low-frequency region, characteristic of Warburg impedance related to lithium-ion diffusion. As summarized in Table 1, the charge-transfer resistance (R_ct) for F-FMMO/G is markedly lower (73.7 Ω) compared to FMMO/G (243 Ω). This substantial reduction in R_ct clearly demonstrates the enhanced electrical conductivity of the fluorine-doped heterostructure, consistent with the improved electronic transport indicated by Hall results and the enhanced defect signal in EPR, which contributes to its superior electrochemical performance.

Table 1
Electrochemical impedance parameters and diffusion coefficients.

Electrode	R_S (Ω)	R_{ct} (Ω)	σ_w	Diffusion coefficient ($cm^2\ s^{-1}$)
FMMO/G	6.93	243	2.05E + 01	2.86E-14
F-FMMO/G	7.1	73.7	9.86E + 01	1.24E-15

Figure 2a compares the cycling behavior at 0.1 C. Both samples exhibit high initial irreversible discharge capacities: 1045 mAh g^{-1} for FMMO/G and 1158 mAh g^{-1} for F-FMMO/G. The corresponding initial cycling curves are presented in Fig. 2b. After the formation cycle, the fluorinated composite stabilizes at ~ 860 mAh g^{-1}, which is the more representative reversible capacity for subsequent cycling. For FMMO/G, the capacity maintains a relatively stable capacity of 1016 mAh g^{-1}, then gradually decays at a rate of approximately 0.2% per cycle over the first 80 cycles. After this point, the decay accelerates to 0.9% per cycle, resulting in a sharp capacity decline. By the 150th cycle, the capacity drops to 360 mAh g^{-1}, which corresponds to only 35% of its initial value. In contrast, the fluorine-doped F-FMMO/G shows a different trend. After the initial capacity drop, the specific capacity gradually increases over the next 50 cycles, at a rate of 0.1% per cycle. This improvement is attributed to enhanced electrolyte infiltration and gradual activation of the electrode surface. Following this activation phase, a slow and steady capacity decay is observed. However, the F-FMMO/G retains significantly better stability than its undoped counterpart. After 150 cycles, it maintains a capacity of 780 mAh g^{-1}, which is approximately 90% of its initial value and demonstrates excellent cycling durability.

The rate performance of both samples is depicted in Fig. 2c, where the behavior under varying current densities appears comparable. The F-FMMO/G electrode exhibits superior rate performance under the same testing conditions. To further evaluate high-rate capabilities, the F-FMMO/G electrode was subjected to extended cycling at 10 C, as shown in Fig. 2d. During initial cycles at 0.1 C, the specific capacity exceeds 900 mAh g^{-1}. Upon increasing the current density to 10 C, the capacity drops rapidly from 480 mAh g^{-1} to 180 mAh g^{-1} within 25 cycles and then stabilizes around 100 mAh g^{-1}. Impressively, this stabilized capacity is sustained for over 200 cycles. When the current density is returned to 0.1 C, the capacity recovers to over 900 mAh g^{-1}, indicating excellent structural robustness and rate-reversible capacity. These results confirm that F-FMMO/G exhibits outstanding rate capability and high structural integrity under extreme cycling conditions.

Figure 3a presents the cyclic voltammetry (CV) curves of FMMO/G and F-FMMO/G electrodes measured at a scan rate of 1 mV s^{-1} within a voltage window of 0.01–3.0 V. FMMO/G exhibits no distinct redox peaks, showing only broad humps, which is characteristic of pseudocapacitive or amorphous-like behavior, consistent with our previous findings[22]. In contrast, the F-FMMO/G electrode displays two well-defined reduction peaks at 1.51 V and 1.26 V, along with corresponding oxidation peaks at 1.54 V and 1.78 V. These redox couples can be identified as follows: the pair at 1.78 V (oxidation) and 1.51 V

(reduction) yields a potential separation (ΔV) of 0.27 V, while the pair at 1.54 V (oxidation) and 1.26 V (reduction) yields a ΔV of 0.28 V. The redox features in this voltage range can be attributed to stepwise conversion of the molybdate-containing phases involving reduction/oxidation of transition-metal centers (Fe/Mn/Mo) together with Li_2O formation/decomposition and interfacial lithium storage on the graphene-coupled composite framework. The appearance of distinct and symmetric redox peaks in F-FMMO/G confirms improved electrochemical reversibility and well-defined redox kinetics after fluorine doping.

Table 2
Hall effect results comparison of FMMO/G and F-FMMO/G.

Anode Material	Temperature (K)	Resistivity (ohm·cm)	Electron Mobility ($cm^2 V^{-1} S^{-1}$)	Carrier Concentration ($1/cm^3$)	R_H ($cm^3 C^{-1}$)
FMMO/G	300	3.77E + 01	8.71E + 01	1.90E + 15	-3.29E + 03
F-FMMO/G	300	3.10E + 01	9.30E + 01	1.88E + 15	-3.72E + 03

To elucidate the intrinsic electronic structure modifications induced by fluorine doping, electron paramagnetic resonance (EPR) spectroscopy and Hall effect measurements were performed. As shown in Fig. 3b, both samples exhibit a prominent EPR signal at g ≈ 2.001, typically attributed to unpaired electrons associated with oxygen vacancies and other defect states. Notably, the F-FMMO/G sample displays a significantly stronger signal than FMMO/G, indicating a higher concentration of paramagnetic centers, primarily oxygen vacancies, introduced by F^- incorporation. This finding is consistent with the XPS analysis, which revealed modulation of Fe valence states, suggesting that fluorine doping effectively engineers the defect chemistry of the material. Complementary Hall effect measurements (Table 2) provide quantitative insight into the electronic transport properties. Both FMMO/G and F-FMMO/G exhibit negative Hall coefficients (R_H), confirming n-type semiconductor behavior with electrons as the dominant charge carriers. Following fluorine doping, the room-temperature resistivity of F-FMMO/G decreases from 3.77×10^1 Ω·cm to 3.10×10^1 Ω·cm, while electron mobility increases from 8.71×10^1 $cm^2 V^{-1} s^{-1}$ to 9.30×10^1 $cm^2 V^{-1} s^{-1}$, while the carrier concentration remains relatively constant (~ 1.9×10^{15} cm^{-3}). These results indicate that the primary role of fluorine doping is not to increase carrier density but to enhance carrier mobility within the lattice. This mobility enhancement is attributed to two key factors: (i) F-induced oxygen vacancies act as donor sites, donating electrons to the conduction band and reducing scattering events; and (ii) local electronic structure modification weakens Fe–O bonds, as evidenced by XPS, thereby lowering the energy barrier for electron hopping. Together, the EPR and Hall effect analyses confirm that fluorine doping functions as an effective electronic modulator. It simultaneously increases the density of active defect states and improves the efficiency of charge transport. This intrinsic conductivity enhancement, coupled with the built-in electric field at the

heterojunction interface, underpins the significantly reduced charge-transfer resistance and outstanding high-rate capability observed in the F-FMMO/G anode.

X-ray photoelectron spectroscopy (XPS) was employed to investigate survey results of F-FMMO/G and the changes in the oxidation states of Fe in FMMO/G and F-FMMO/G, as shown in Fig. 4, with the corresponding quantitative data summarized in the inset table of Fig. 4a and Table 3. The F1s signal is detected with an atomic concentration of 0.9 at. %, confirming successful fluorine incorporation into the material. The Fe/Mn atomic ratio is approximately 1.05, consistent with the nominal stoichiometry of $Fe_{x}Mn_{1-x}MoO_4$ ($x \approx 0.5$). The relatively high carbon content (61.77 at. %) originates from both the intrinsic graphene component and surface-adsorbed adventitious carbon, which is commonly observed in air-exposed carbon-containing samples.

The Fe 2p spectra of both samples can be deconvoluted into characteristic Fe^{2+} and Fe^{3+} doublets, indicating the coexistence of mixed valence states. Notably, the Fe^{2+}/Fe^{3+} ratio increases from 1.59 in FMMO/G to 1.71 in F-FMMO/G, demonstrating that fluorine doping effectively modulates the Fe valence distribution. This increase in the Fe^{2+} fraction is consistent with the higher initial specific capacity observed for the fluorine-doped sample. In addition to the change in valence states, a systematic shift of Fe 2p binding energies toward lower values is observed after fluorine doping, indicating a weakened Fe–O bonding environment. The reduced bond strength lowers the energy barrier for Li^+ insertion and extraction, thereby facilitating lithium-ion intercalation kinetics. Furthermore, the modified surface electronic structure is expected to promote more favorable interfacial charge-transfer processes, contributing to the enhanced electrochemical performance of the F-FMMO/G electrode.

Table 3
Fe 2p XPS valence distribution.

Electrode	orbit	B.E.	XPS AREA	AREA RATIO
FMMO/G	$Fe^{2+}2p_{3/2}$	710.8	10300	Fe^{2+}/Fe^{3+}=1.59
	$Fe^{2+}2p_{1/2}$	724	5150	
	$Fe^{3+}2p_{3/2}$	712.8	6468	
	$Fe^{3+}2p_{1/2}$	726.5	3234	
F-FMMO/G	$Fe^{2+}2p_{3/2}$	710.46	5724	Fe^{2+}/Fe^{3+}=1.71
	$Fe^{2+}2p_{1/2}$	723.46	2862	
	$Fe^{3+}2p_{3/2}$	712.53	3346	
	$Fe^{3+}2p_{1/2}$	726.02	1673	

The high-resolution transmission electron microscopy (HR-TEM) images in Fig. 5 reveal the stacked nanosheet structure of the F-FMMO/G composite. Despite being composed of two heterophase structures, well-defined crystalline fringes are clearly observed, indicating the high crystallinity of the final product. In Fig. 5a, lattice fringes corresponding to the (101) and (112) planes of $Mn_2Mo_3O_8$ (JCPDS 34–510) are observed, intersecting at an angle of approximately 89°, consistent with the expected crystallographic orientation. Figure 5b shows the presence of the (220) plane of $FeMoO_4$ (JCPDS 22–628), while Fig. 5c reveals the (002) and (101) planes of $Mn_2Mo_3O_8$. Selected area electron diffraction (SAED) analysis, shown in Fig. 5d, further supports these findings. The diffraction pattern exhibits clear and distinct spots arranged in concentric rings, which, together with other evidence provided earlier, confirms the polycrystalline nature of the heterostructure. Specifically, the first and third rings correspond to the (002) and (112) planes of $Mn_2Mo_3O_8$, while the second ring is assigned to the (220) plane of $FeMoO_4$. These results collectively validate the coexistence of both crystalline phases in the fluorine-doped composite, which can provide abundant contact regions for charge transfer and mechanical buffering during cycling. In addition, a thin amorphous layer is observed at the outer edge of the HR-TEM images. This layer is expected to facilitate lithium-ion insertion and extraction by providing a more accessible surface and flexible interface between the electrode and electrolyte, potentially contributing to the improved electrochemical kinetics of the F-FMMO/G anode.

Theoretical Calculation Results

To investigate the atomic-scale charge redistribution and electronic structure at the heterojunction interface, we constructed an interface model between the $FeMoO_4$ (220) and $Mn_2Mo_3O_8$ (112) planes.

Differential charge density analysis, shown in Fig. 6a, illustrates the spatial distribution of electron transfer at the interface. The cyan and yellow isosurfaces represent regions of electron depletion and accumulation, respectively. A clear electron accumulation is observed on the $Mn_2Mo_3O_8$ side, while electron depletion occurs on the adjacent $FeMoO_4$ region. This asymmetric charge redistribution indicates spontaneous electron transfer from $FeMoO_4$ to $Mn_2Mo_3O_8$ upon contact, generating a built-in electric field directed from the electron-rich $Mn_2Mo_3O_8$ to the electron-deficient $FeMoO_4$. This interfacial electric field is critical for enhancing charge separation and facilitating Li^+ migration during electrochemical cycling. It also contributes to the reduced interfacial charge-transfer resistance, in agreement with the EIS results (Table 1).

Furthermore, the electronic band structure of the heterojunction was analyzed, as shown in Fig. 6b. Notably, the calculated band gap for the integrated $FeMoO_4/Mn_2Mo_3O_8$ heterojunction is approximately 0 eV, indicating a quasi-metallic character. The valence band maximum (VBM, − 0.9884 eV) and conduction band minimum (CBM, − 0.9854 eV) are nearly degenerate, resulting in an almost negligible energy barrier for electron excitation. This near-zero band gap is of critical importance for charging transport, as it allows thermal excitation of electrons from the valence band to the conduction band with

minimal energy input. Consequently, the intrinsic carrier concentration is expected to be several orders of magnitude higher than that of conventional semiconductors with typical band gaps exceeding 1 eV. This dramatically enhanced bulk electronic conductivity offers a fundamental explanation for the superior rate performance of the F-FMMO/G composite, enabling rapid and efficient electron transport throughout the electrode under high-current operating conditions.

Collectively, the DFT results reveal a dual enhancement mechanism that underlies the exceptional electrochemical performance of the F-FMMO/G composite. First, interfacial engineering plays a critical role: the spontaneous charge transfer at the $FeMoO_4/Mn_2Mo_3O_8$ interface establishes a built-in electric field, which effectively facilitates both ion and electron transport across the heterojunction and significantly lowers interfacial resistance. Second, bulk property modulation is achieved through heterostructure formation, which induces a quasi-metallic electronic structure characterized by a near-zero band gap. This leads to a substantial increase in intrinsic electronic conductivity throughout the bulk material. The synergistic interplay between interfacial charge modulation and enhanced bulk conductivity, enabled by the rational design of the heterojunction architecture, is the key to the ultrahigh-rate capability demonstrated by the F-FMMO/G anode. This dual mechanism provides a compelling design strategy for the development of next-generation high-performance lithium-ion battery materials.

Conclusions

In summary, a fluorine-doped $Fe_xMn_{1-x}MoO_4$/graphene (F-FMMO/G) heterojunction nanocomposite was successfully developed as an ultrahigh-rate anode material for lithium-ion batteries (LIBs) through a synergistic design strategy. This approach effectively combines the advantages of heterojunction engineering and fluorine anion doping to address the intrinsic limitations of conventional conversion-type anodes. The in-situ formation of a heterojunction between $FeMoO_4$ and $Mn_2Mo_3O_8$ phases generates a built-in electric field that significantly enhances charge-transfer kinetics, as evidenced by the substantial reduction in charge-transfer resistance (73.7 Ω for F-FMMO/G vs. 243 Ω for the undoped sample). Simultaneously, fluorine doping modulates the local bonding environment by weakening Fe–O interactions, thereby facilitating Li^+ diffusion and improving both structural robustness and interfacial stability during cycling. As a result, the F-FMMO/G anode delivers outstanding electrochemical performance, including an ultrahigh reversible capacity of 1158 mAh g^{-1} at 0.1 C, excellent cycling stability with 90% capacity retention after 150 cycles, and superior rate capability, maintaining structural integrity under prolonged operation at 10 C with rapid capacity recovery. Complementary density functional theory (DFT) calculations reveal a dual enhancement mechanism: spontaneous interfacial charge transfer generates a favorable electric field for ion/electron transport, while heterostructure formation leads to a quasi-metallic electronic structure with a near-zero band gap, significantly improving bulk conductivity. This work not only introduces a high-performance anode material but also elucidates the synergistic mechanism between interfacial and bulk-level modifications. The design principle demonstrated here—integrating interfacial charge modulation with electronic structure

engineering via elemental doping—offers a powerful and generalizable strategy for the development of next-generation high-power energy storage systems.

Experimental

Material Synthesis

$Fe_xMn_{1-x}MoO_4$/G and F-$Fe_xMn_{1-x}MoO_4$/G composites were synthesized via a solvothermal method. First, 1 mmol of $(NH_4)_6Mo_7O_{24}$ (Fisher Chemical, Laboratory Grade) was dissolved in a mixed solvent of ethylene glycol (EG) and deionized water (EG: H_2O = 2:1 by volume) to prepare solution A, followed by stirring for 30 minutes. Separately, 3.5 mmol of $FeCl_2{\cdot}4H_2O$ (Sigma-Aldrich, 99.5%) and 3.5 mmol of $MnCl_2{\cdot}H_2O$ (Sigma-Aldrich, 99.5%) were dissolved in 30 mL of distilled water to form solution B. After stirring solution B for 1 hour, it was added dropwise to solution A under vigorous stirring. The mixture was then stirred continuously for 4 hours. Subsequently, 10 mL of a pre-prepared graphene oxide (GO) dispersion (2 mg mL^{-1}) was added dropwise to the resulting solution, followed by an additional hour of stirring. The GO was synthesized according to a previously reported method[23]. Then, 0.48 mmol of NH_4F (Fisher Chemical, > 98%) was added, and the mixture was stirred for another 5 minutes to ensure homogeneity before the solvothermal reaction. The final solution was transferred into a 100 mL Teflon-lined stainless-steel autoclave, sealed, and maintained at 180 ℃ for 20 hours. After the reaction, the autoclave was allowed to cool naturally to room temperature. The resulting precipitate was collected, washed thoroughly with deionized water several times, and dried at 60 ℃ under vacuum for 12 hours. The dried product was then sintered at 650 ℃ for 8 hours in an argon atmosphere to obtain the fluorine-doped heterojunction composite, designated as F-FMMO/G. For comparison, a non-doped control sample (FMMO/G) was synthesized using the same procedure, excluding the addition of NH_4F.

Material Characterization

Thermal stability was assessed using thermogravimetric-differential scanning calorimetry (TG-DSC) on a NETZSCH STA 449C instrument. Samples were heated in an N_2 atmosphere at a rate of 5 ℃ min^{-1}. Crystal structure analysis was conducted via powder X-ray diffraction (XRD) using a Bruker D8 Advance diffractometer with Cu Kα radiation (λ = 0.154 nm) over a 2θ range of 10° to 80°. Electrochemical properties were evaluated using cyclic voltammetry (CV) and electrochemical impedance spectroscopy (EIS), performed on a Chenhua CHI660E workstation. The EIS tests used an AC amplitude of ± 5 mV over a frequency range of 10^2 to 10^6 Hz. X-ray photoelectron spectroscopy (XPS) was carried out on a ThermoFisher ESCALAB Xi+ instrument with Al Kα radiation (hv = 1486.6 eV), under a base pressure of 8 × 10^{-10} Pa. All binding energies were referenced to the C 1s peak at 284.8 eV. Raman spectra were obtained using a Thermo DXi confocal Raman spectrometer with a 532 nm excitation source at 300 K. Electron paramagnetic resonance (EPR) spectra were recorded on a Bruker E500 system. The microwave frequency: X-band, ranging from 9.3 GHz to 9.9 GHz (with automatic tuning). Magnetic field range: 0 to

1.4 Tesla (0–14,000 Gauss). All measurements were conducted at room temperature unless otherwise specified.

Electrochemical Performance Characterization

The electrochemical performance of FMMO/G and F-FMMO/G was evaluated using 2032-type coin half-cells. The electrolyte consisted of 1.0 M $LiPF_6$ in a 1:1 (v/v) mixture of ethylene carbonate (EC) and diethyl carbonate (DEC). A polypropylene microporous membrane (Celgard 2500) was used as the separator. Electrodes were prepared by blending active material, Super P conductive carbon, and poly (vinylidene fluoride) (PVDF) binder in a weight ratio of 8:1:1. The resulting slurry was coated onto copper foil, dried overnight at 65 ℃ under vacuum, and punched into circular electrodes with a diameter of 14 mm. The weight of active material per anode is 5 ~ 6 mg. Coin cells were assembled in an argon-filled glovebox. Galvanostatic charge–discharge tests were carried out on a LAND CT2001A multichannel battery tester (Wuhan, China) at various current densities within a voltage window of 0.01–3 V (vs. Li^+/Li) at room temperature.

Theoretical Calculation

All first-principles calculations were performed within the framework of density functional theory (DFT) using the Vienna Ab initio Simulation Package (VASP 6.3.0)[24–26]. The exchange-correlation interactions were treated using the generalized gradient approximation (GGA) with the Perdew–Burke–Ernzerhof (PBE) functional[27]. Interactions between core and valence electrons were described using the projector augmented wave (PAW) method with standard pseudopotentials[28]. A 3 × 2 × 1 Monkhorst–Pack k-point grid was used for Brillouin zone sampling, and a plane-wave cutoff energy of 500 eV was applied. The atomic structures were fully relaxed until the total energy convergence threshold reached 10^{-6} eV and the maximum residual force on each atom was less than 0.03 eV/Å. To account for the localized nature of d-electrons in the transition metals, the DFT + U method was employed. Effective Hubbard U values were set to 2.5 eV for both Mn and Fe, and 2.0 eV for Mo.

Declarations

Acknowledgments

We would like to thank the funding support from Excellent Youth Project of Hunan Provincial Department of Education (Project No.: 23B0772).

Author contributions statement

T.L. conceived and designed the experiments; T.L., X.C., H.C., and C.H. performed the synthesis and characterization; T.L., P.Y., and W.T. conducted the electrochemical measurements and analyzed the

data; T.L. and W.T. performed the DFT calculations; T.L. and W.T. wrote the manuscript; T.L. and W.T. supervised the project. All authors reviewed and approved the final manuscript.

Data availability: Data will be made available on request from the corresponding author upon reasonable request.

Competing interests: The authors declare no conflicts of interest.

References

1. Zhang, D. et al. MnO Nanoparticles Attached to S, N Co-Doped Carbon Skeleton as a High-Rate Performance Anode Material. *Molecules* **29**, 4306. 10.3390/molecules29184306 (2024). Concisely Constructing S, F Co-Modified.
2. Du, J. et al. Graphene Doped with Transition Metal Oxides: Enhancement of Anode Performance in Lithium-Ion Batteries. *Metals* **15**, 387. 10.3390/met15040387 (2025).
3. Armand, M. & Tarascon, J. M. Building better batteries. *nature* 451, 652–657 (2008).
4. Goodenough, J. B. & Park, K. S. The Li-ion rechargeable battery: a perspective. *J. Am. Chem. Soc.* **135**, 1167–1176 (2013).
5. Yu, X. Y., Hu, H., Wang, Y., Chen, H. & Lou, X. W. Ultrathin MoS_2 nanosheets supported on N-doped carbon nanoboxes with enhanced lithium storage and electrocatalytic properties. *Angew. Chem.* **127**, 7503–7506. 10.1002/anie.201502117 (2015).
6. Hu, L. et al. $CoMn_2O_4$ spinel hierarchical microspheres assembled with porous nanosheets as stable anodes for lithium-ion batteries. *Sci. Rep.* **2**, 986. 10.1038/srep00986 (2012).
7. Zhang, L., Wu, H. B. & Lou, X. W. Iron-oxide-based advanced anode materials for lithium-ion batteries. *Adv. Energy Mater.* **4**, 1300958. 10.1002/aenm.201300958 (2014).
8. Mai, L., Tian, X., Xu, X., Chang, L. & Xu, L. Nanowire electrodes for electrochemical energy storage devices. *Chem. Rev.* **114**, 11828–11862. 10.1021/cr500177a (2014).
9. Wang, Y., Zeng, H. C. & Lee, J. Y. Highly reversible lithium storage in porous SnO_2 nanotubes with coaxially grown carbon nanotube overlayers. *Adv. Mater.* **18**, 645–649. 10.1002/adma.200501883 (2006).
10. Hoster, H. E., Zhang, G., Yu, L., Wu, H. B. & Lou, D. X. W. Formation of $ZnMn_2O_4$ ball-in-ball hollow microspheres as a high-performance anode for lithium-ion batteries. *Adv. Mater.* **24**, 4609–4613. 10.1002/adma.201201779 (2012).
11. Yuan, C. et al. Ultrathin mesoporous $NiCo_2O_4$ nanosheets supported on Ni foam as advanced electrodes for supercapacitors. *Adv. Funct. Mater.* **22**, 4592–4597. 10.1002/adfm.201200994 (2012).
12. Liu, T. et al. Approaching theoretical specific capacity of iron-rich lithium iron silicate using graphene-incorporation and fluorine-doping. *J. Mater. Chem. A*. **10**, 4006–4014. 10.1039/D1TA09417C (2022).

13. Wang, J., Zhang, Q., Han, P., Luo, J. & Peng, K. Q. An S-Infused/S, F-Codoped PVDF-Derived Carbon as a High-Performance Anode for Sodium-Ion Batteries. *Materials* **18**, 4018. 10.3390/ma18174018 (2025).
14. Etacheri, V., Marom, R., Elazari, R., Salitra, G. & Aurbach, D. Challenges in the development of advanced Li-ion batteries: a review. *Energy Environ. Sci.* **4**, 3243–3262. 10.1039/clee01598b (2011).
15. Xu, K. Electrolytes and interphases in Li-ion batteries and beyond. *Chem. Rev.* **114**, 11503–11618. 10.1021/cr500003w (2014).
16. Wu, H. B., Chen, J. S., Hng, H. H. & Lou, X. W. D. Nanostructured metal oxide-based materials as advanced anodes for lithium-ion batteries. *Nanoscale* **4**, 2526–2542. 10.1039/C2NR11966H (2012).
17. Bruce, P. G., Scrosati, B. & Tarascon, J. M. Nanomaterials for rechargeable lithium batteries. *Angew. Chem. Int. Ed.* **47**, 2930–2946. 10.1002/anie.200702505 (2008).
18. Massé, R. C., Liu, C., Li, Y., Mai, L. & Cao, G. Energy storage through intercalation reactions: electrodes for rechargeable batteries. *Natl. Sci. Rev.* **4**, 26–53. 10.1093/nsr/nww093 (2017).
19. Yadav, J. K., Rani, B., Saini, P. & Dixit, A. Rechargeable iron-ion (Fe-ion) batteries: recent progress, challenges, and perspectives. *Energy Adv.* **3**, 927–944. 10.1039/D4YA00101J (2024).
20. Yuan, L. et al. High-performance electrodes based on metal-organic framework-templated bimetallic molybdate on graphene-decorated nickel foam. *J. Electroanal. Chem.* **119791** 10.1016/j.jelechem.2026.119791 (2026).
21. Huu, H. T. & Im, W. B. Facile green synthesis of pseudocapacitance-contributed ultrahigh capacity $Fe_2(MoO_4)_3$ as an anode for lithium-ion batteries. *ACS Appl. Mater. Interfaces*. **12**, 35152–35163. 10.1021/acsami.0c11862 (2020).
22. Liu, T., Liu, Y., Niu, C. & Chao, Z. S. Pseudocapacitive contribution in amorphous $FeVO_4$ cathode for lithium-ion batteries. *ChemElectroChem* 9, e202101493, (2022). 10.1002/celc.202101493
23. Li, Z. F. et al. Fabrication of high-surface-area graphene/polyaniline nanocomposites and their application in supercapacitors. *ACS Appl. Mater. Interfaces*. **5**, 2685–2691. 10.1021/am4001634 (2013).
24. Vienna, U. o. *Vienna Ab initio Simulation Package (VASP 6.2.0)*, (2020). https://www.vasp.at/
25. Kresse, G. & Furthmüller, J. Efficient iterative schemes for ab initio total-energy calculations using a plane-wave basis set. *Phys. Rev. B*. **54**, 11169. 10.1103/PhysRevB.54.11169 (1996).
26. Kresse, G. & Joubert, D. From ultrasoft pseudopotentials to the projector augmented-wave method. *Phys. Rev. B*. **59**, 1758. 10.1103/PhysRevB.59.1758 (1999).
27. Perdew, J. P., Burke, K. & Ernzerhof, M. Generalized gradient approximation made simple. *Phys. Rev. Lett.* **77**, 3865 (1996).
28. Blochl, P., Blöchl, E. & Blöchl, P. E. Projected augmented-wave method. *Phys. Rev. B*. **50**, 17953–17979. 10.1103/PhysRevB.50.17953 (1994).

Figures

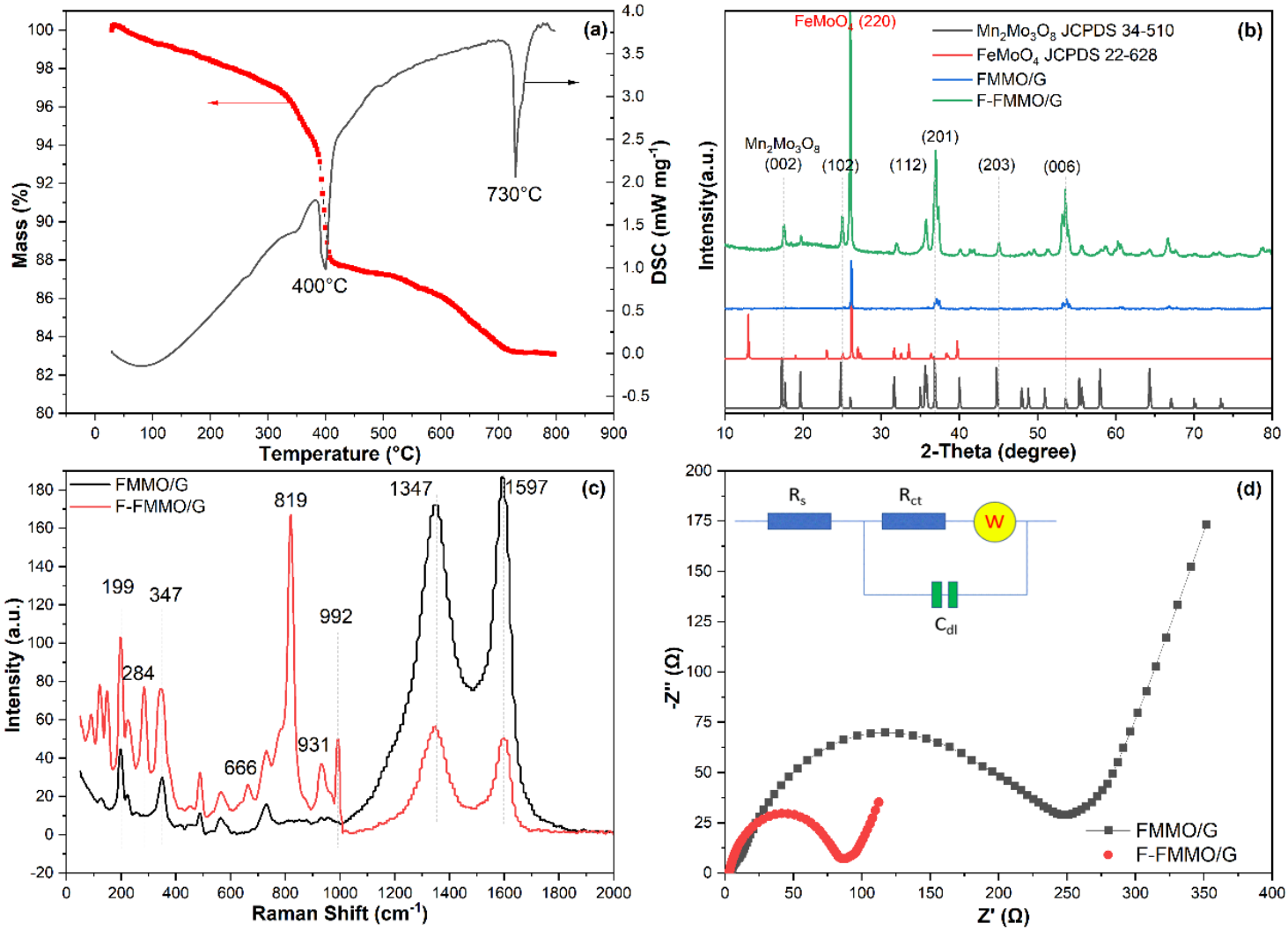

Figure 1

(a) Thermogravimetric-Differential Scanning Calorimetry (TG-DSC) of the precursor. (b) X-ray diffraction (XRD) patterns of FMMO/G and F-FMMO/G sintered at 650 °C and standard patterns ($FeMoO_4$ JCPDS 22-628 and $Mn_2Mo_3O_8$ JCPDS 34-510). Increment: 0.02°, scan rate: 5° min^{-1}. (c) Raman spectroscopy of FMMO/G and F-FMMO/G. (d) Electrochemical impedance spectroscopy (EIS) of FMMO's new cells. Amplitude: 5 mV, frequency range: 1MHz-0.01Hz. The inset is the equivalent electrical circuit of all the fittings used in the software ZSimpWin.

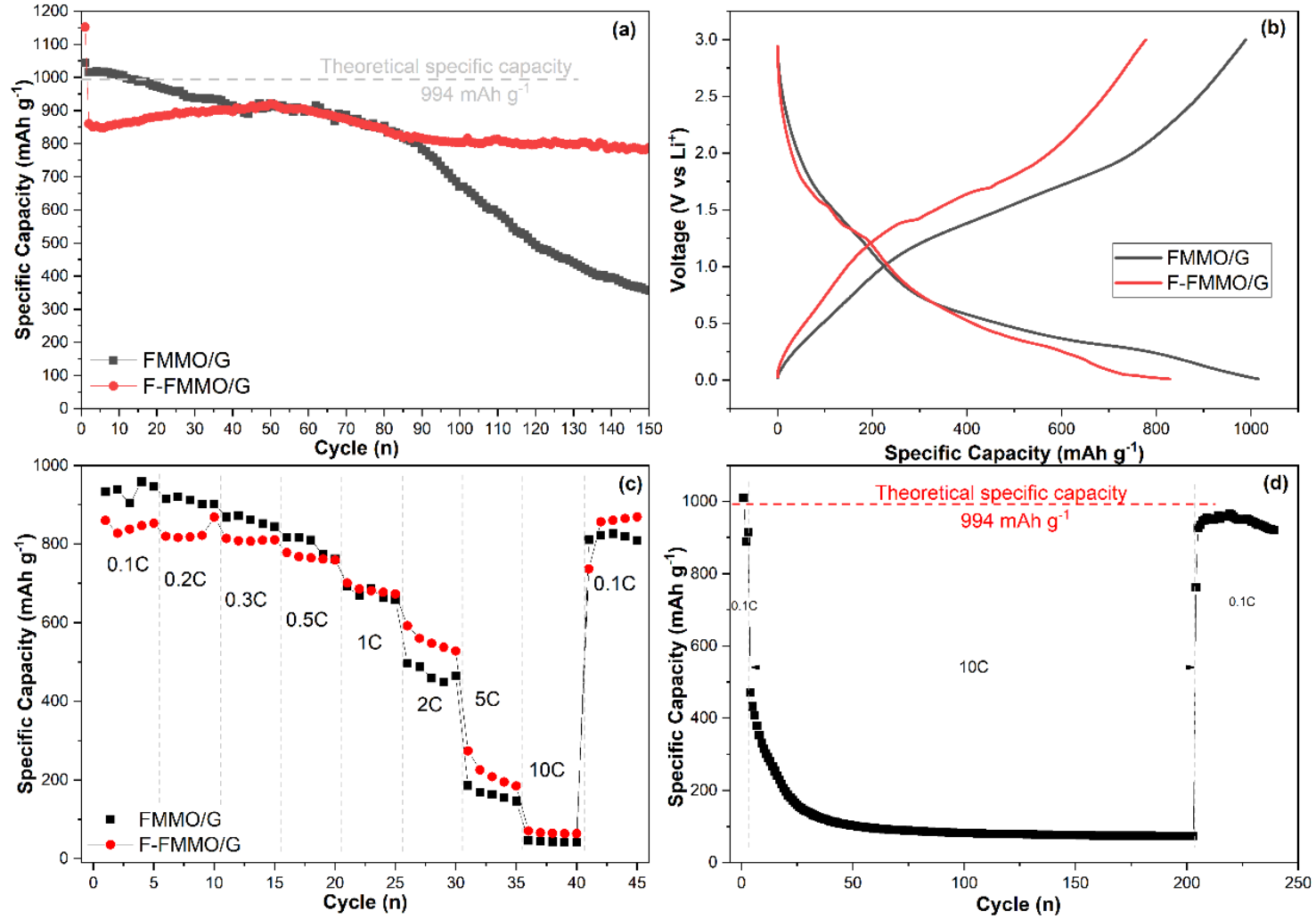

Figure 2

Electrochemical performance. (a) Cycle life comparison as specific capacity of FMMO/G and F-FMMO/G at 0.1 C. (b) Cycle curve comparison of FMMO/G and F-FMMO/G at 0.1 C after initial cycles. (c) Rate performance of FMMO/G and F-FMMO/G. (d) 10C rate performance of F-FMMO/G.

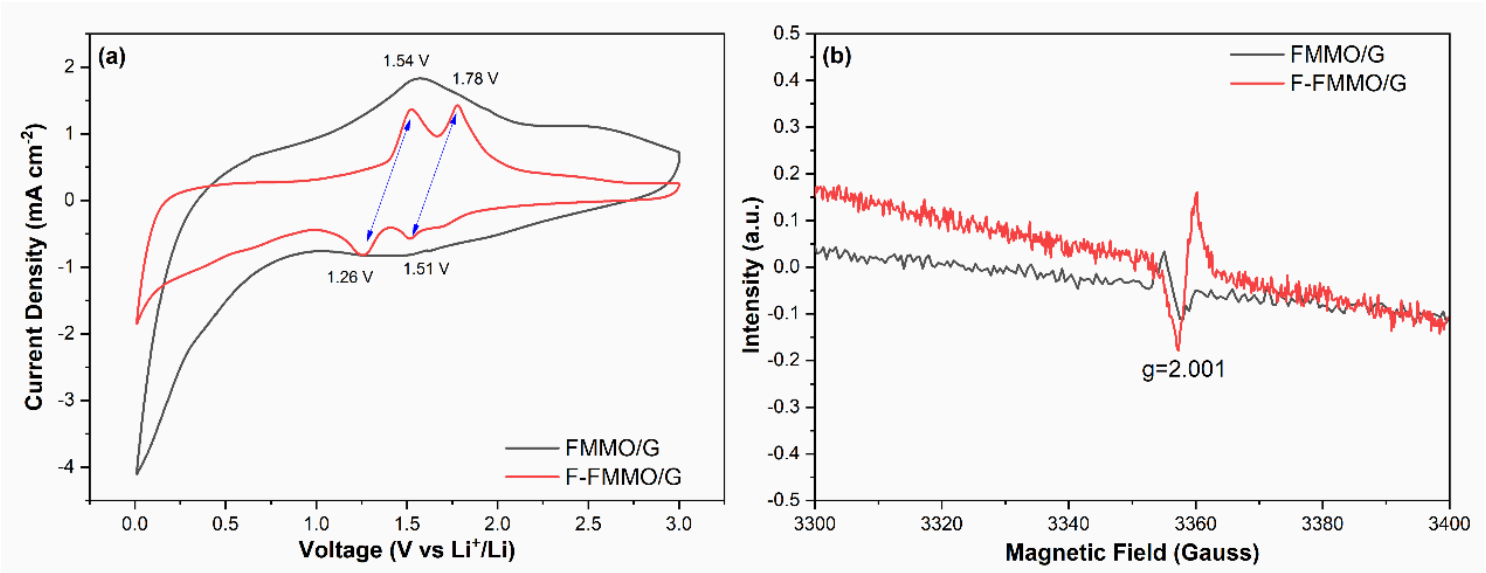

Figure 3

(a) CV curves of FMMO/G and F-FMMO/G at the scan rate of 1 mV s^{-1}. Voltage window: 0.01-3.0 V. (b) EPR spectroscopy analysis results of FMMO/G and F-FMMO/G.

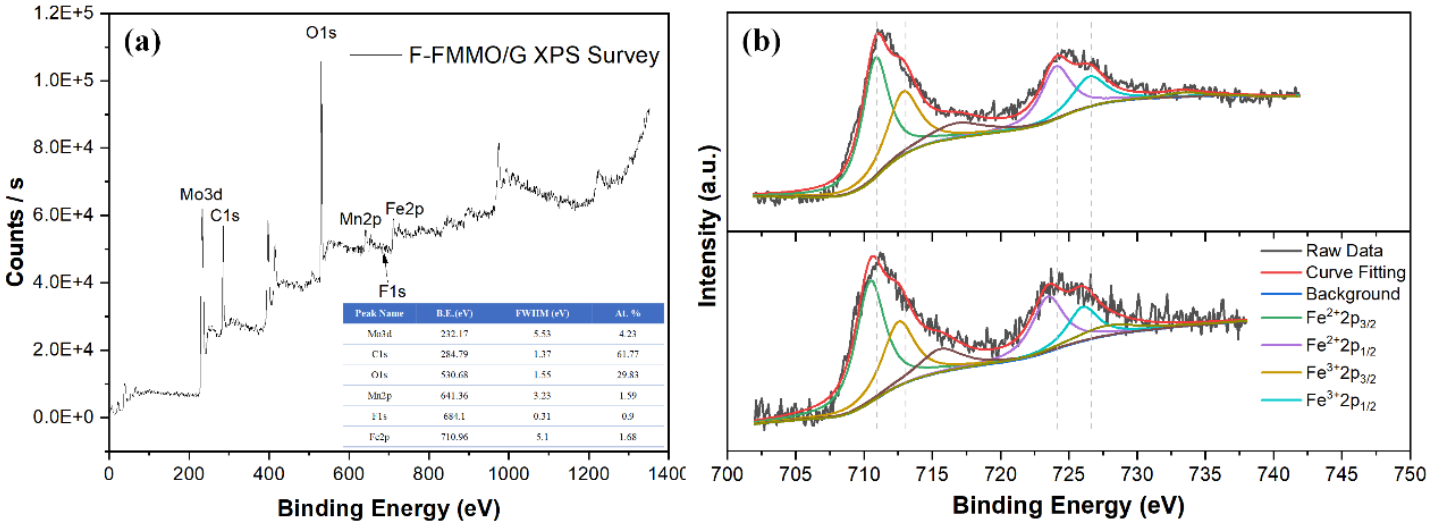

Figure 4

XPS spectroscopy analysis results. (a) XPS survey of F-FMMO/G. Inset table is the atomic percentage comparison. (b) Fe 2p XPS spectrum comparison of FMMO/G and F-FMMO/G.

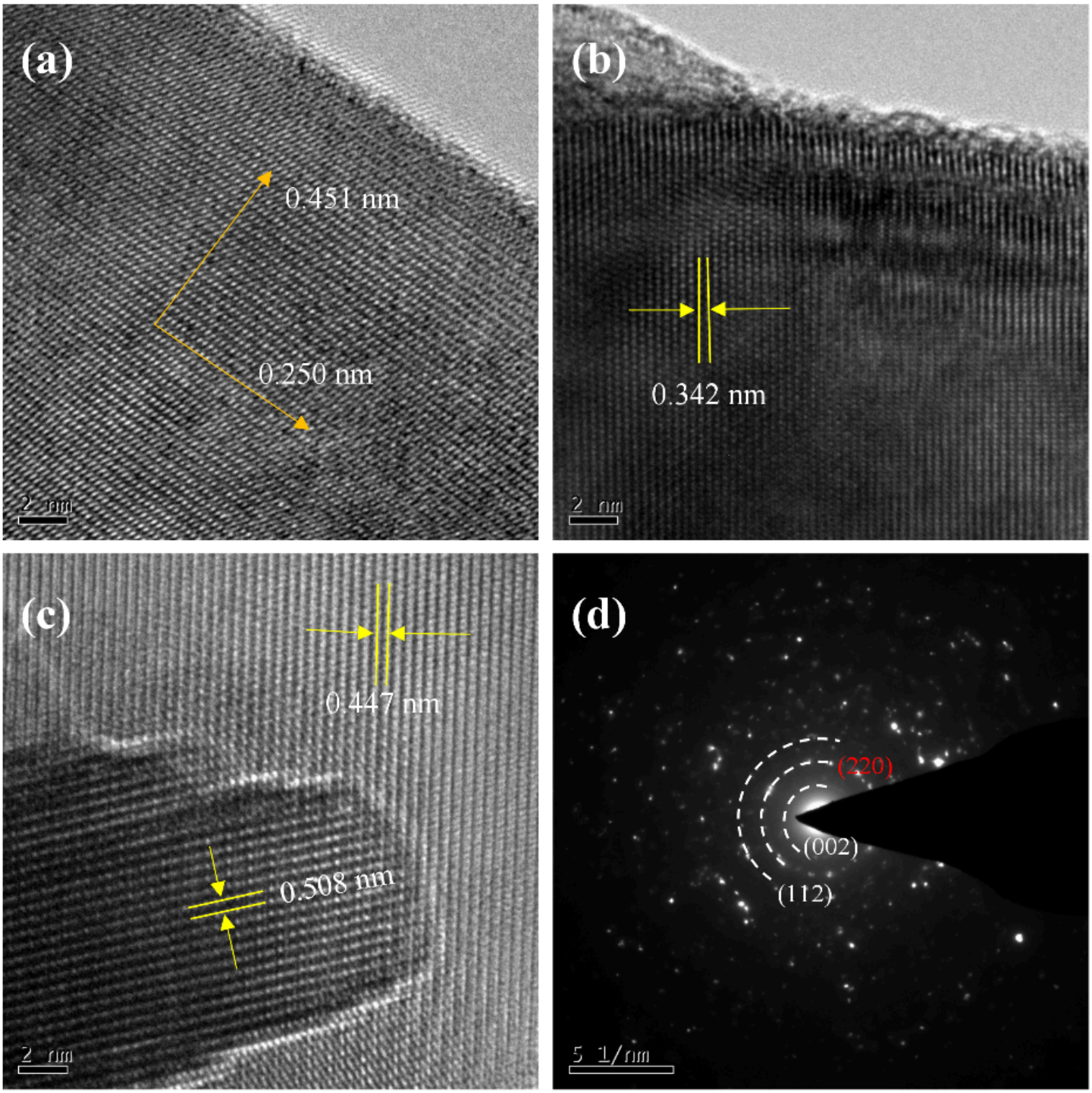

Figure 5

HRTEM of F-FMMO/G (a-c). Scale: 2 nm. (d) SAED of F-FMMO/G. Scale: 5 1/nm.

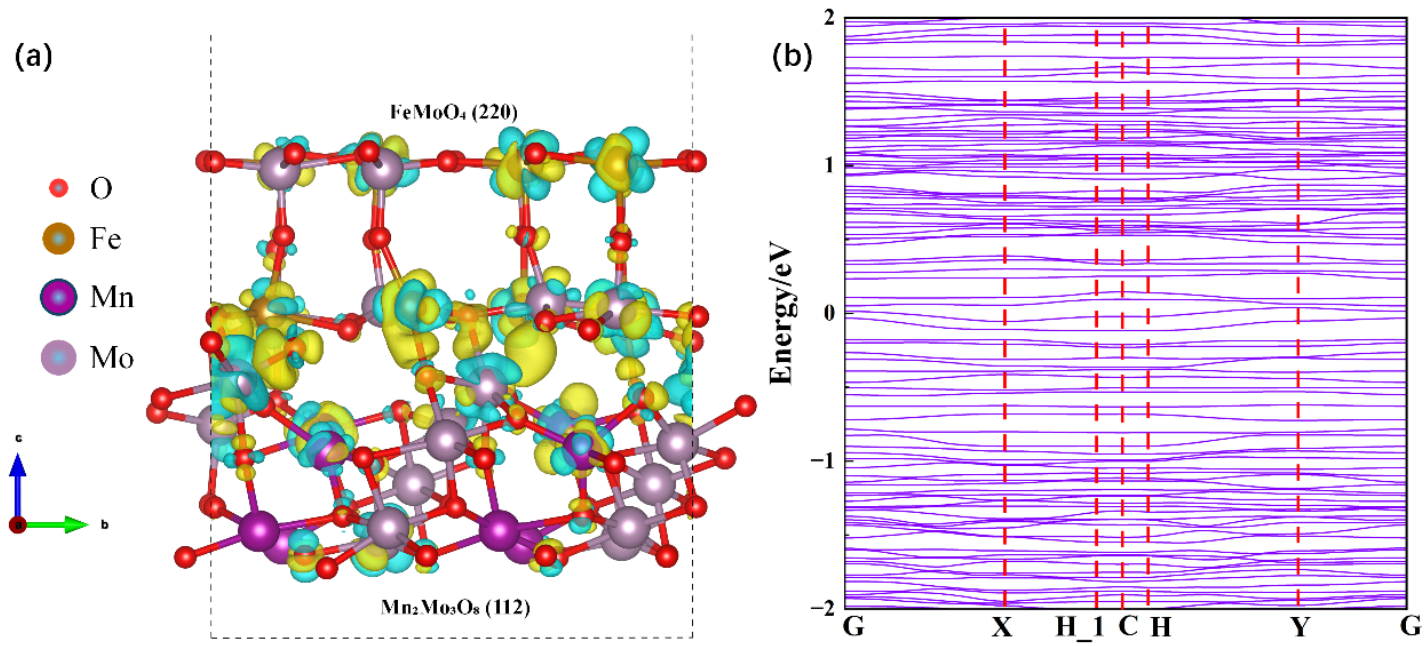

Figure 6

DFT results of F-FMMO/G composite. (a) Differential charge density of the $FeMoO_4$ (220)/ $Mn_2Mo_3O_8$ (112) heterojunction interface. (b) Energy bands of $FeMoO_4$ (220) and $Mn_2Mo_3O_8$ (112) planes.